Transcranial recording of electrophysiological neural activity in the rodent brain *in vivo* using functional photoacoustic imaging of near-infrared voltage-sensitive dye

JEEUN KANG[1,2], HAICHONG K. ZHANG[1,2], SHILPA D. KADAM[3], JULIE FEDORKO[2], HEATHER VALENTINE[2], ADARSHA P. MALLA[4], PING YAN[5], JIN U. KANG[1], ARMAN RAHMIM[2], ALBERT GJEDDE[2,6], LESLIE M. LOEW[5], DEAN F. WONG[2,4,6,7,8], EMAD M. BOCTOR[1,2]*

[1] *Whiting School of Engineering, Johns Hopkins University, Baltimore, MD 21218, USA*
[2] *Russell H. Morgan Department of Radiology and Radiological Science, Johns Hopkins Medical Institutions, Baltimore, MD 21287, USA*
[3] *Department of Neurology, Hugo W. Moser Research Institute at Kennedy Krieger, Johns Hopkins Medical Institutions, Baltimore, MD 21205, USA*
[4] *Solomon H. Snyder Department of Neuroscience, Johns Hopkins Medical Institutions, Baltimore, MD 21205, USA*
[5] *Department of Cell Biology, University of Connecticut Health, Farmington, CT 06030, USA*
[6] *Department of Neuroscience, University of Copenhagen, Copenhagen 2200, Denmark*
[7] *Department of Psychiatry and Behavioral Sciences, Johns Hopkins Medical Institutions, Baltimore, MD 21287, USA*
[8] *Department of Neurology, Johns Hopkins Medical Institutions, Baltimore, MD 21205, USA.*
**eboctor1@jhmi.edu*

Abstract: Minimally-invasive monitoring of electrophysiological neural activities in real-time—that enables quantification of neural functions without a need for invasive craniotomy and the longer time constants of fMRI and PET—presents a very challenging yet significant task for neuroimaging. In this paper, we present proof-of-concept *in vivo* functional PA (fPA) imaging of chemoconvulsant rat seizure model with intact scalp using a fluorescence quenching-based cyanine voltage-sensitive dye (VSD) characterized by a lipid vesicle model mimicking different levels of membrane potential variation. The framework also involves use of a near-infrared VSD delivered through the blood-brain barrier (BBB), opened by pharmacological modulation of adenosine receptor signaling. Using normalized time-frequency analysis on temporal PA sequences, the neural activity in the seizure group was distinguished from those of the control groups. Electroencephalogram (EEG) recording confirmed the changes of severity and frequency of brain activities, induced by chemoconvulsant seizures of the rat brain. The findings demonstrate that fPA imaging of fluorescence quenching-based VSD is a promising tool for *in vivo* recording of deep brain activities in the rat brain, thus excluding the need of invasive craniotomy.

References

1. K. J. Friston, "Modalities, Modes, and Models in Functional Neuroimaging," Science **326**(5951), 399–403 (2009).
2. M. E. Raichle and M. A. Mintun, "Brain work and brain imaging," Annu. Rev. Neurosci. **29**(1), 449–476 (2006).
3. N. V. Vanitha, "Positron emission tomography in neuroscience research," ANS **18**(2), 36 (2011).
4. M. E. Raichle, "Behind the scenes of functional brain imaging: a historical and physiological perspective," Proc. Natl. Acad. Sci. U.S.A. **95**(3), 765–772 (1998).
5. N. K. Logothetis, "What we can do and what we cannot do with fMRI - ProQuest," Nature (2008).
6. M. G. Berman, J. Jonides, and D. E. Nee, "Studying mind and brain with fMRI," Social cognitive and affective neuroscience **1**(2), 158–161 (2006).
7. E. M. C. Hillman, "Optical brain imaging in vivo: techniques and applications from animal to man," J. Biomed. Opt. **12**(5), 051402–051402–28 (2007).

8. A. Devor, S. Sakadžić, V. J. Srinivasan, M. A. Yaseen, K. Nizar, P. A. Saisan, P. Tian, A. M. Dale, S. A. Vinogradov, M. A. Franceschini, and D. A. Boas, "Frontiers in optical imaging of cerebral blood flow and metabolism," J. Cereb. Blood Flow Metab. **32**(7), 1259–1276 (2012).
9. C. Heo, H. Park, Y.-T. Kim, E. Baeg, Y. H. Kim, S.-G. Kim, and M. Suh, "A soft, transparent, freely accessible cranial window for chronic imaging and electrophysiology," Sci Rep **6**(1), 27818 (2016).
10. G. E. Strangman, Z. Li, and Q. Zhang, "Depth sensitivity and source-detector separations for near infrared spectroscopy based on the Colin27 brain template," PLoS ONE **8**(8), e66319 (2013).
11. A. Torricelli, D. Contini, A. Pifferi, M. Caffini, R. Re, L. Zucchelli, and L. Spinelli, "Time domain functional NIRS imaging for human brain mapping," NeuroImage **85 Pt 1**, 28–50 (2014).
12. L. V. Wang and S. Hu, "Photoacoustic tomography: in vivo imaging from organelles to organs," Science **335**(6075), 1458–1462 (2012).
13. X. Wang, Y. Pang, G. Ku, X. Xie, G. Stoica, and L. V. Wang, "Noninvasive laser-induced photoacoustic tomography for structural and functional in vivo imaging of the brain," Nat Biotechnol **21**(7), 803–806 (2003).
14. L. Nie, X. Cai, K. Maslov, A. Garcia-Uribe, M. A. Anastasio, and L. V. Wang, "Photoacoustic tomography through a whole adult human skull with a photon recycler," J. Biomed. Opt. **17**(11), 110506 (2012).
15. W. Li, R. Chen, J. Lv, H. Wang, Y. Liu, Y. Peng, Z. Qian, G. Fu, and L. Nie, "In Vivo Photoacoustic Imaging of Brain Injury and Rehabilitation by High-Efficient Near-Infrared Dye Labeled Mesenchymal Stem Cells with Enhanced Brain Barrier Permeability," Adv Sci (Weinh) **5**(2), 1700277–11 (2018).
16. X. L. Deán-Ben, G. Sela, A. Lauri, M. Kneipp, V. Ntziachristos, G. G. Westmeyer, S. Shoham, and D. Razansky, "Functional optoacoustic neuro-tomography for scalable whole-brain monitoring of calcium indicators," Light Sci Appl **5**(12), e16201–7 (2016).
17. B. Rao, R. Zhang, L. Li, J.-Y. Shao, and L. V. Wang, "Photoacoustic imaging of voltage responses beyond the optical diffusion limit," Sci Rep **7**(1), 2560 (2017).
18. H. K. Zhang, P. Yan, J. Kang, D. S. Abou, H. N. D. Le, A. K. Jha, D. L. J. Thorek, J. U. Kang, A. Rahmim, D. F. Wong, E. M. Boctor, and L. M. Loew, "Listening to membrane potential: photoacoustic voltage-sensitive dye recording," J. Biomed. Opt. **22**(4), 045006 (2017).
19. G. Paxinos and C. Watson, *The Rat Brain in Stereotaxic Coordinates*, Seventh edition (Elsevier Academic Press, 2014).
20. J. S. Treger, M. F. Priest, R. Iezzi, and F. Bezanilla, "Real-time imaging of electrical signals with an infrared FDA-approved dye," Biophysj **107**(6), L09–L012 (2014).
21. I. Martišienė, R. Mačianskienė, R. Treinys, A. Navalinskas, M. Almanaitytė, D. Karčiauskas, A. Kučinskas, R. Grigalevičiūtė, V. Zigmantaitė, R. Benetis, and J. Jurevičius, "Voltage-Sensitive Fluorescence of Indocyanine Green in the Heart," BPJ **110**(3), 723–732 (2016).
22. K. Jurkat-Rott and F. Lehmann-Hom, "The patch clamp technique in ion channel research," Current Pharmaceutical Biotechnology **5**(4), 387–395 (2004).
23. V. Rosilio, "How Can Artificial Lipid Models Mimic the Complexity of Molecule–Membrane Interactions?" Advances in Biomembranes and Lipid Self-Assembly (2018).
24. F. Mazur, M. Bally, B. Städler, and R. Chandrawati, "Liposomes and lipid bilayers in biosensors," Advances in Colloid and Interface Science **249**, 88–99 (2017).
25. W. F. Paxton, P. T. McAninch, K. E. Achyuthan, S. H. R. Shin, and H. L. Monteith, "Monitoring and modulating ion traffic in hybrid lipid/polymer vesicles," Colloids and Surfaces B: Biointerfaces **159**, 268–276 (2017).
26. R. R. Ramnath, K. Strange, and P. A. Rosenberg, "Neuronal injury evoked by depolarizing agents in rat cortical cultures," Neurosci Res **51**(4), 931–939 (1992).
27. M. Takahashi, S. Y. Liou, and M. Kunihara, "Ca(2+)- and Cl(-)-dependent, NMDA receptor-mediated neuronal death induced by depolarization in rat hippocampal organotypic cultures," Brain Res. **675**(1), 249–256 (1995).
28. M. D. Archer, *Electrochemistry, Past and Present*, **Chapter 8. Genesis of the Nernst Equation** (American Chemical Society, 1989), **390**, pp. 115–126.
29. W. Löscher, "Animal Models of Seizures and Epilepsy: Past, Present, and Future Role for the Discovery of Antiseizure Drugs," Neurochem. Res. **42**(7), 1873–1888 (2017).
30. H. F. Bradford, "Glutamate, GABA and epilepsy," Progress in Neurobiology **47**(6), 477–511 (1995).
31. A. J. Carman, J. H. Mills, A. Krenz, D.-G. Kim, and M. S. Bynoe, "Adenosine receptor signaling modulates permeability of the blood-brain barrier," Journal of Neuroscience **31**(37), 13272–13280 (2011).
32. S. L. Jacques and S. Prahl, *Extinction Coefficient of Melanin* (OMLC (https://omlc.org/spectra/melanin/extcoeff.html), 2013).
33. K. Nowak, E. Mix, K. Nowak, U. Strauss, J. Gimsa, R. Benecke, K. K. Sriperumbudur, and U. Gimsa, "Optimizing a Rodent Model of Parkinson's Disease for Exploring the Effects and Mechanisms of Deep Brain Stimulation," Parkinson's Disease **2011**(2754), 1–19 (2011).
34. I. Sigal, M. M. Koletar, D. Ringuette, R. Gad, M. Jeffrey, P. L. Carlen, B. Stefanovic, and O. Levi, "Imaging brain activity during seizures in freely behaving rats using a miniature multi-modal imaging system," Biomed. Opt. Express **7**(9), 3596–14 (2016).
35. H. Siemen, D. Colas, H. C. Heller, O. Brüstle, and R. A. R. Pera, "Pumilio-2 function in the mouse nervous system," PLoS ONE **6**(10), e25932 (2011).

36. D. A. Adler, S. Ammanuel, J. Lei, T. Dada, T. Borbiev, M. V. Johnston, S. D. Kadam, and I. Burd, "Circadian cycle-dependent EEG biomarkers of pathogenicity in adult mice following prenatal exposure to in utero inflammation," Neurosci Res **275**, 305–313 (2014).
37. M. V. Johnston, S. Ammanuel, C. O'Driscoll, A. Wozniak, S. Naidu, and S. D. Kadam, "Twenty-four hour quantitative-EEG and in-vivo glutamate biosensor detects activity and circadian rhythm dependent biomarkers of pathogenesis in Mecp2 null mice," Front Syst Neurosci **8**(JUNE), 118 (2014).
38. M. A. Goss-Sampson and A. Kriss, "Effects of pentobarbital and ketamine-xylazine anaesthesia on somatosensory, brainstem auditory and peripheral sensory-motor responses in the rat," Lab. Anim. **25**(4), 360–366 (1991).
39. G. Ordek, J. D. Groth, and M. Sahin, "Differential effects of ketamine/xylazine anesthesia on the cerebral and cerebellar cortical activities in the rat," Journal of Neurophysiology **109**(5), 1435–1443 (2013).
40. H. Goldman, R. F. Berman, H. Hazlett, and S. Murphy, "Cerebrovascular responses to pentylenetetrazol: time and dose dependent effects," Epilepsy Res. **12**, 227–242 (1992).
41. A. Nehlig, M. Vergnes, R. Waydelich, E. Hirsch, R. Charbonne, C. Marescaux, and J. Seylaz, "Absence seizures induce a decrease in cerebral blood flow: Human and animal data," J. Cereb. Blood Flow Metab. **16**(1), 147–155 (1996).
42. Y. Hoshi and M. Tamura, "Dynamic changes in cerebral oxygenation in chemically induced seizures in rats: study by near-infrared spectrophotometry," Brain Res. **603**(2), 215–221 (1993).
43. T. Zhang, J. Zhou, R. Jiang, H. Yang, P. R. Carney, and H. Jiang, "Pre-seizure state identified by diffuse optical tomography," Sci Rep **4**(1), 113–10 (2014).
44. P. M. Lewis, R. H. Thomson, J. V. Rosenfeld, and P. B. Fitzgerald, "Brain Neuromodulation Techniques: A Review," Neuroscientist **22**(4), 1073858416646707–421 (2016).
45. J. Kang, S. D. Kadam, J. S. Elmore, B. J. Sullivan, H. Valentine, A. P. Malla, M. M. Harraz, A. Rahmim, J. U. Kang, L. M. Loew, M. Baumann, A. A. Grace, A. Gjedde, E. M. Boctor, and D. F. Wong, "Transcranial photoacoustic imaging of NMDA-evoked focal circuit dynamics in rat forebrain," bioRxiv **308585**, 1–26 (2018).
46. J. Kang, S. D. Kadam, H. K. Zhang, H. Valentine, J. Fedorko, D. F. Wong, and E. M. Boctor, "Transcranial recording of stimulated neuronal activity variation *in vivo* using photoacoustic voltage-sensitive dye imaging," in (2017), **10494-53**.
47. Y. Tufail, A. Yoshihiro, S. Pati, M. M. Li, and W. J. Tyler, "Ultrasonic neuromodulation by brain stimulation with transcranial ultrasound," Nat Protoc **6**(9), 1453–1470 (2011).
48. P.-C. Chu, H.-L. Liu, H.-Y. Lai, C.-Y. Lin, H.-C. Tsai, and Y.-C. Pei, "Neuromodulation accompanying focused ultrasound-induced blood-brain barrier opening," Sci Rep **5**, 15477 (2015).

1. Introduction

The quantification and monitoring of brain function is a major goal of neuroscience and research into the underlying mechanisms of the working brain [1,2]. Towards this objective, several modalities have been introduced for the purpose of neuroimaging; however, existing methods have limitations. Positron emission tomography (PET) provides high molecular resolution and pharmacological specificity, but suffers from low spatial and temporal resolution [3,4]. Functional magnetic resonance imaging (fMRI) provides higher spatial resolution of brain activity; however, the recorded blood-oxygenation level dependent (BOLD) signal has comparatively low temporal resolution and involves uncertain interpretation [5,6]. Optical imaging approaches have been used to monitor the brain function of small animals but have limited dynamic ranges and cover only superficial tissue depths because of light scattering and absorbance during penetration of biological tissue [7,8]. These optical approaches require invasive craniotomy for imaging of deeper brain region, with problematic long-term consequences such as dural regrowth, greater likelihood of inflammatory cascade initiation, and lack of translational practicality to non-human primate and ultimately to human studies, including those for neuropsychiatric disorders [9]. Near-infrared spectroscopy (NIRS) monitors brain function non-invasively in real-time (~1ms) for deep biological tissues (~several mm), but suffers from poor spatial resolution (~1cm) at those depths [10,11]. Therefore, minimally-invasive monitoring of electrophysiological brain activities in real-time remains a task at hand in neuroimaging, with the aim to quantify brain functions at high spatial resolution in the depths of brain tissue, without need for invasive craniotomy.

To overcome the current challenges, photoacoustic (PA) imaging has been investigated as a promising hybrid modality that provides the molecular contrast of brain function with

acoustic transcranial penetration and high spatial resolution [12,13]. In PA imaging, radio-frequency (RF) acoustic pressure is generated, depending on the thermo-elastic property and light absorbance of a target illuminated by pulsed laser, and it is detected by an ultrasound transducer. Based on this mechanism, several studies have presented the capability of transcranial PA imaging [14,15]. Additionally, several PA approaches have been recently applied to detect electrophysiological brain activities in both tomographic and microscopic imaging modes; Deán-Ben et al. presented *in vivo* whole brain monitoring of zebrafish using real-time PA tomography of a genetically encoded calcium indicator, GCaMP5G [16]. Ruo et al. reported PA imaging *in vivo* of mouse brain responses to electrical stimulation and 4-aminopyridine-induced epileptic seizures by means of hydrophobic anions such as dipicrylamine (DPA) [17]. However, these studies used voltage sensing in the visible spectral range (488nm and 530nm for GCaMP5G; 500nm and 570nm for DPA), which is not optimal for recording deep tissue neural activity because of the optical attenuation. To address this, we recently presented a novel mechanism of near-infrared cyanine voltage sensitive dye (VSD) based on selective fluorescence quenching on membrane potential variations [18].

Here, we propose *in vivo* functional PA (fPA) imaging of chemoconvulsant rat seizure model with intact scalp using our near-infrared cyanine VSD characterized by a lipid vesicle model mimicking various membrane potential levels. As a step towards minimally-invasive external imaging in primates and human brains, the results demonstrate that the fPA imaging of the fluorescence quenching VSD mechanism is a promising approach to the recording deep brain activities in rat brain, without need for craniotomy.

2. Methods

2.1 fPA VSD imaging setup.

An ultrasound research system was comprised by a 128-channel 1-dimensional ultrasound linear array transducer (L14-5/38) connected to a real-time data acquisition system (SonixDAQ, Ultrasonix Corp., Canada). To induce the PA signals, pulsed laser light was generated by a second-harmonic (532nm) Nd:YAG laser pumping an optical parametric oscillator (OPO) system (Phocus Inline, Opotek Inc., USA). The tunable range of the laser system was 690-900nm and the maximum pulse repetition frequency was 20Hz. The laser pulse was fed into a fiber optic bundle delivering to bifurcated outlets, each 40mm long and 0.88mm wide (Fig. 1a). The customized, 3-D printed shell fixes the ultrasound probe between the outlets of the bifurcated fiber optic bundle outlets for evenly distributed laser energy density in lateral direction. The bifurcated output beams were overlapped at 20mm depth. The PA probe was located at around 2.2mm from bregma to obtain the cross-section of motor cortexes (Fig. 1c). The distance between fPA probe and rat skin surface was 20 mm, and the resultant energy density was at 3.5mJ/cm^2, which is far below the maximum permissible exposure (MPE) of skin to laser radiation by the ANSI safety standards. A wavelength of 790nm was used, at which the light energy was sufficiently absorbed by the near-infrared VSD, i.e., IR780 perchlorate, more than by hemoglobin contents. Also, probing at this wavelength prevented the undesired error by time-variant oxygen change, being at the isosbestic point of Hb and HbO_2 absorption spectra (Fig. 1b). Fig. 1c presents a representative cross-sectional PA image of a rat brain. The dotted white outlines for the brain and motor cortex were drawn based on the rat brain atlas [19]. See the appendix for *in vivo* imaging performance.

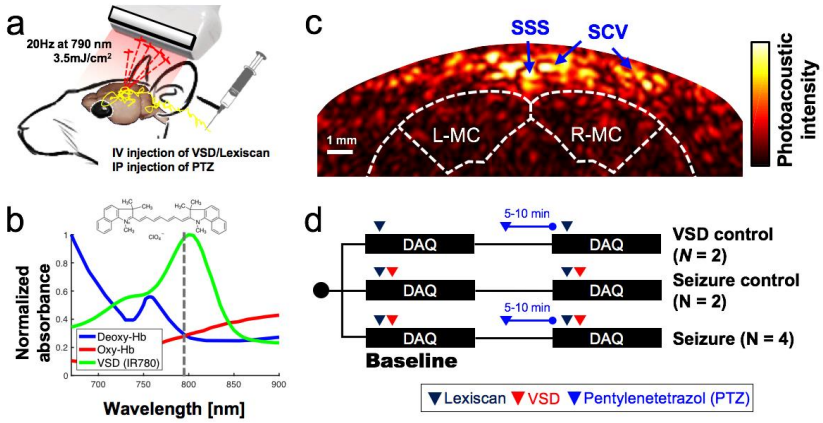

Fig. 1. Transcranial VSD sensing setup using fPA imaging system: (a) schematic diagram of experimental setup; (b) absorbance spectra of VSD, deoxy- and oxy-hemoglobin. Dotted line indicates the wavelength used in *in vivo* experiment, i.e., 790nm; (c) cross-sectional PA image of cerebral cortex; (d) *in vivo* experimental protocol. SSS: Superior sagittal sinus; SCV: Superior cortical veins. L-MC/R-MC: left/right motor cortex. Note that the outlines for brain and motor cortex in Fig. 1c was drawn based on the rat brain atlas (Bregma 2.2mm) [19]. The success of seizure induction on motor cortex was confirmed by tonic-clonic movements in the fore and hind-limbs of the anesthetized rat during the experiments (See Movie 1).

2.2 Fluorescence quenching-based near-infrared voltage-sensitive dye.

Several cyanine VSDs have been proposed as markers for real-time electrical signal detection [20] and fluorescence tracking of electrical signal propagation on a heart [21]. Recently we presented the mechanism of action of a cyanine VSD for fPA imaging [18]. The discussed mechanism of VSD proposes a suppressive PA contrast when neuronal depolarization occurs, while yielding a reciprocal contrast for fluorescence. In the present proof-of-principle study, we used the fluorescence quenching-based near-infrared cyanine VSD, IR780 perchlorate (576409, Sigma-Aldrich Co. LLC, MO, United States) with the analogous chemical structure of PAVSD800-2 in our previous study. Note that the response time of the given VSD redistribution mechanism through cell membrane should be slow in sub-second scale as presented in our previous study [18].

2.3 Lipid vesicle phantom preparation for VSD validation.

The physicochemical and biophysical studies regarding the interaction of exogenous molecules with a biological membrane have been extensively investigated using a single cell patch clamping [22] or using lipid vesicle models for precise control and measurement of cell membrane potential [23-25]. In this study, we are based on the lipid vesicle model considering our VSD mechanism in a tissue-scale between extracellular space and the cytoplasm of polarized cells as a function of membrane potential. The single cell patch clamping is optimized for an individual cell, rather than the cluster of cells. There is also an approach to control a cell membrane potential using valinomycin and varying the external K^+ on a cell suspension, while being monitored in fluorescence or PA microscopy [17]. However, this treatment for membrane potential control may affect the biological state of living cells by causing them to swell and bleb in practice [26,27]. On the contrary, the lipid vesicle model is free from these concerns, and more consistent measurements could be allowed between lipid vesicle model and translational *in vivo* experiments by using the identical cross-sectional imaging system described in section 2.1.

The lipid vesicle model was prepared using the same procedure as in Zhang et al [18]; 25-mg soybean phosphatidyl-choline (type II) suspended in 1mL of K^+ buffer was used as the lipid vesicles. This vesicle contains 100mM K_2SO_4 and 20mM HEPES. The suspension was vortexed for 10 min, and followed by 60 min of sonication within bath-type sonicator to yield

a translucent vesicle suspension. A Na^+ buffer was also prepared, containing100mM Na_2SO_4 and 20mM HEPES. Afterwards, 25:1, 50:1, and 100:1 K^+ gradients across vesicle membrane were established with 2.5µL, 5.0µL, and 10.0µL of lipid vesicle suspensions respectively added to 1mL of Na^+ buffers. In the lipid vesicle model prepared, negative membrane potential (polarized state) was mimicked by adding 2.5µL of 10µM valinomycin—a K^+ specific ionophore, thereby K^+ ions were transported from inside to outside of vesicle membranes. On the other hand, 2.5µL of 1mM gramicidin, a nonspecific monovalent cation ionophore, enabled Na^+ cations to move from outside to inside of vesicle membranes to short circuit the membrane potential (depolarized state). From these controls, our near-infrared VSD positively charged can move in and out through the vesicle membrane, leading to the change in fluorescence quenching depending on their aggregation status. From this lipid vesicle model, we expected the logarithmic change in membrane potential levels (i.e., -83mV, -102mV, and -120mV based on the Nernst equation [28]). This will yield a corresponding suppressive PA intensity change. The quantum yields of the VSD in depolarized states (Φ'_F) were estimated based on the equations in our previous literature (Eqs. 8 and 9 in [18]).

2.4 Animal preparation.

For the proposed *in vivo* experiments. 8-9-week-old male Sprague Dawley rats weighing 275-390g were used (Charles Rivers Laboratory, Inc., MA, United States). The use of animals for the proposed *in vivo* protocol was approved by the Institutional Research Board Committee of Johns Hopkins Medical Institute (RA16M225). All animals were anesthetized by intraperitoneal injection with a ketamine (100mg/ml) / xylazine (20mg/ml) cocktail. (3:1 ratio based on body weight at 1ml/kg). The hair was shaved from the scalp of each rat for better optical and acoustic coupling. The head of the anesthetized rat was fixed to a stable position using a standard stereotaxic device. This fixation procedure was required to prevent any unpredictable movement during the fPA recording.

2.5 Chemoconvulsant seizure induction.

Penetylenetetrazole (PTZ), a gamma-aminobutyric acid (GABA) A receptor antagonist was used to induce acute seizures in the animals [29]. PTZ suppresses the inhibitory effects of GABA, thus leading to generation of synchronized depolarizations of neurons in form of epileptiform discharges and seizures [30]. To induce global episodic acute seizures in rat brain, an intraperitoneal (IP) injection of PTZ (45mg/ml) was utilized based on the animal's body weight in a volume of 1ml/kg. Subsequent doses were given if no acute motor seizure was observed in 5-10 min after the first PTZ injection. Generally, 1-2 doses were sufficient to induce the motor seizures in our experiments.

2.6 Pharmacological treatment for VSD delivery into blood-brain-barrier.

The lumen of the brain microvasculature consists of brain endothelial cells, and the blood-brain barrier (BBB) is comprised of their tight junctions to control the chemical exchange between neural cells and cerebral nervous system (CNS). In this study, the penetration through BBB were achieved with a pharmacological method using FDA-approved regadenoson (Lexiscan, Astellas Pharma US, Inc. IL, United States). This modulates the Adenosine receptor signaling at BBB layer [31]. The dosage and IV administration method indicated by the manufacturer was utilized: A volume of 150µl of the standard concentration of 0.08mg/1ml was given to each animal regardless of the weight, followed by 150µl flush of 0.9% sodium chloride for injection. The experimental protocol was designed based on the pharmacological assumption that the VSD delivery through BBB would occur during the Lexiscan's biological half-life, i.e., 2-3 min. The efficiency of the pharmacological BBB opening was evaluated by the frozen-section histopathological analysis with near-infrared fluorescence microscopy. Three different groups were compared in this study: (1) Negative control: VSD-/Lexiscan-; (2) Control: VSD+/Lexiscan-; (3) BBB opening: VSD+/Lexiscan+.

2.7 In vivo experimental protocol.

Fig. 1d shows the detailed protocol for VSD control, seizure control, and seizure groups. Note that each data acquisition was performed for 10 min to cover the biological half-life of Lexiscan for VSD delivery (2-3 min). Each dosing protocol of Lexiscan and VSD was as follows: Through the jugular vein catheter port located in the neck, 150µl of Lexiscan 0.4mg/5ml concentration was injected, and 300µl of VSD was subsequently administrated at 0.1mg/ml concentration, followed by 150µl of saline solution flush. The seizure control (n = 2) and seizure groups (n = 4) were designed to distinguish the chemoconvulsant effects on neural activity: both groups received VSD and Lexiscan, but only seizure group had IP injection of PTZ (45mg/ml/kg). The induction of seizure was confirmed by monitoring motor seizure, and another dose of PTZ was injected when no motor seizure was observed in 5-10 min. In particular, the success of the rat seizure model was determined by the behavioral observation to identify the tonic-clonic movements in whisker, fore and hind-limbs of the anesthetized rat. Once the seizure is developed, the behavioral seizure activity was maintained for entire time domain (0 – 10 min) in all the data sets presented in this paper. The VSD control group (n = 2) was designed to validate the inability of Lexiscan and PTZ to generate any bias on fPA neural activity detection. In this group, the baseline was obtained with the Lexiscan dosage, and subsequence data set was obtained during the chemoconvulsant seizure with secondary Lexiscan dosage without VSD.

2.8 Criteria for selecting region-of-interest.

The coronal sections of interest were selected to include motor cortices at bregma 2.2mm, at which the synchronized depolarizations of neurons are confirmed by behavioral observation of motor seizure (See Movie 1). In the superficial depth, the signals from superior sagittal sinus (SSS) and superior cortical veins (SCV) are dominant as they contain abundant blood context. Skin surface was less obvious as the melanin contents, a major absorber in scalp, has low absorbance at near-infrared range [32]. Therefore, we used our criteria for localizing brain tissue region using the relative information to SSS and brain atlas by Paxinos [19]. In axial direction, there are four layers between SSS and brain tissue. The SSS is in the middle of dura mater (300µm) which is above the arachnoid (75µm), subarachnoid space (750µm), and pia mater (75µm) layers covering a rat brain [33]. Therefore, the expectable distance between SSS and brain atlas map should be 1,050µm, and motor cortex is extended at 3-4mm from the brain surface (bregma 2.2–3.2mm [19]). From the anatomical criteria, entire brain region was selected as the region-of-interest (ROI) to reject any subjective bias (See the appendix 5.2 for the representative examples of ROI selection).

2.9 Normalized time-frequency analysis.

Fig. 2 demonstrates the flow chart of our normalized time-frequency analysis method based on a short-time Fourier transform (STFT) to detect the suppressive VSD contrast in rat brain. In addition, the method includes several considerations: It has been well known that the chemoconvulsant seizure perturbs the hemodynamics. Specifically, Sigal et al. presented that each motor seizure event in same rodent seizure model produces hemodynamic changes extended in few tens of seconds, which would extend up to 0.1Hz in frequency domain [34]. To exclude this, the high-pass filtering is applied on the PA intensity in temporal direction before performing STFT analysis. On the other hand, the features in electroencephalogram (EEG) of seizure activity broadly extends in frequency range from few Hz to several tens of Hz [35], at which the suppressive VSD mechanism in PA imaging will be activated. From the STFT spectrogram, we employed the frequency normalization procedures to fairly evaluate how much fractional PA contrast have presented over at the frequency range compared to that at the baseline spectrogram.

- **Step 1: Reconstruction of PA image sequence** using a delay-and-sum beamforming for the radio-frequency (RF) channel data averaged for 2-sec duration (40 frames) with 0.25-sec interval (5 frames interval). This lead to 4-Hz refreshing rate, and enables the frequency analysis up to 2Hz with high sensitivity. The higher imaging speed would be

redundant considering slow VSD response in sub-second scale. The signal envelope was detected for the bandwidth 1 - 5MHz;

- **Step 2: High-pass filtering** at 0.2-Hz cutoff frequency in temporal direction at each pixel of envelope-detected PA signal to exclude the seizure-induced hemodynamic changes;
- **Step 3: Short-time Fourier transform (STFT)** at each image pixel point with an analysis window across 40 temporal samples. PA(t, f) denotes a STFT spectrogram at a specific time point t;
- **Step 4: Frequency-domain normalization** by the averaged intensity at low-frequency band f_L (i.e., 0.3-0.5Hz) at each t: $\mathrm{PA}(t, \underline{f}) = \log_{10}(\mathrm{PA}(t, f) / E\{\mathrm{PA}(t, f)\}_{f_L})$, where PA($t$, f) and PA(t, $\underline{f}$) are the PA sequence before and after the normalization. This procedure is to fairly evaluate the amount of suppression at high-frequency range (0.5-2Hz) relative to the reference intensity at f_L. The logarithm procedure is to present the PA intensity in negative decibel level with an emphasis on suppressive PA contrast;
- **Step 5: Baseline normalization**: $\mathrm{PA}(\underline{t}, \underline{f}) = \mathrm{PA}(t, \underline{f})/\mathrm{PA}_0(\underline{f})$, in which the $\mathrm{PA}_0(t, \underline{f})$ is the reference spectrum time-averaged for 5-10-min period in the baseline phase. In this step, the suppressive VSD contrast is converted into positive contrast in PA($\underline{t}$, $\underline{f}$) – More suppressive contrast relative to the baseline would yield higher PA($\underline{t}$, $\underline{f}$);
- **Step 6: fPA quantification of neural activity.** A neural activity index at each pixel is defined by a PA($\underline{t}$, $\underline{f}$) projected over 0.5-2Hz range: $(E\{\mathrm{PA}(\underline{t}, \underline{f})\}_{\underline{f}=0.5-2\mathrm{Hz}} - 1) \times 100$. This reflects how much fractional suppression have produced compared to the reference STFT spectrum. Repeat steps 1 – 6 until all the pixels in brain cross-section are processed.

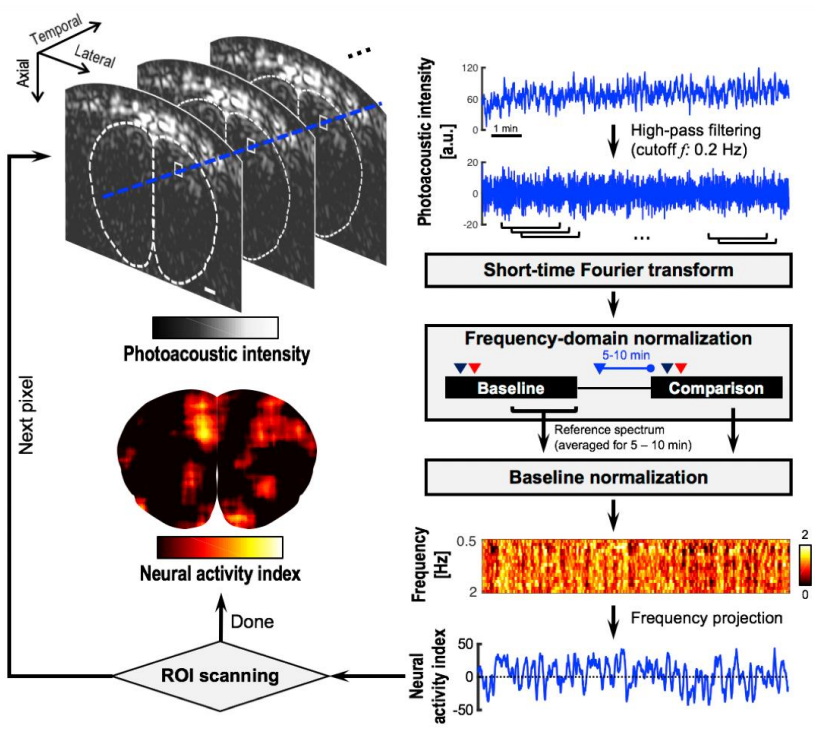

Fig. 2. Flow chart of the short-time Fourier transform (STFT)-based normalized time-frequency analysis method. The dotted contour is boundary of brain tissue drawn based on rat brain atlas. White bar indicates 1 mm.

2.10 EEG validation of neural seizure activity.

To obtain the EEG records of electrical spike discharges that originated from brain tissue, sub-dermal scalp EEG recording electrodes were located at the corresponding locations on

motor cortex (See the Fig. 9a), the schematic of the rat cranium (three electrodes, 1 recording and 1 reference over motor cortex, 1 ground electrode over rostrum). The EEG signal at motor cortex was recorded with the identical preparation procedures in fPA imaging including animal preparation, administration of VSD, Lexiscan, and PTZ, time duration for recording, and interval between sequences in the protocol. Data acquisition was done using Sirenia software (Pinnacle Technologies Inc., Kansas, United States) with synchronous video capture. Briefly, the data acquisition and conditioning system had a 14-bit resolution, sampling rates of 400Hz, high pass filters of 0.5Hz and low pass filters of 60Hz. The files were stored in .EDF format and scored manually for protocol stages using real time annotations added to the recording during the experiments. EEG power for 10 sec epoch displays within the scoring software package was done using an automated module in Sirenia. Further details of our proposed EEG data acquisition and analysis used in this study are as presented in previous studies [36,37].

3. Results

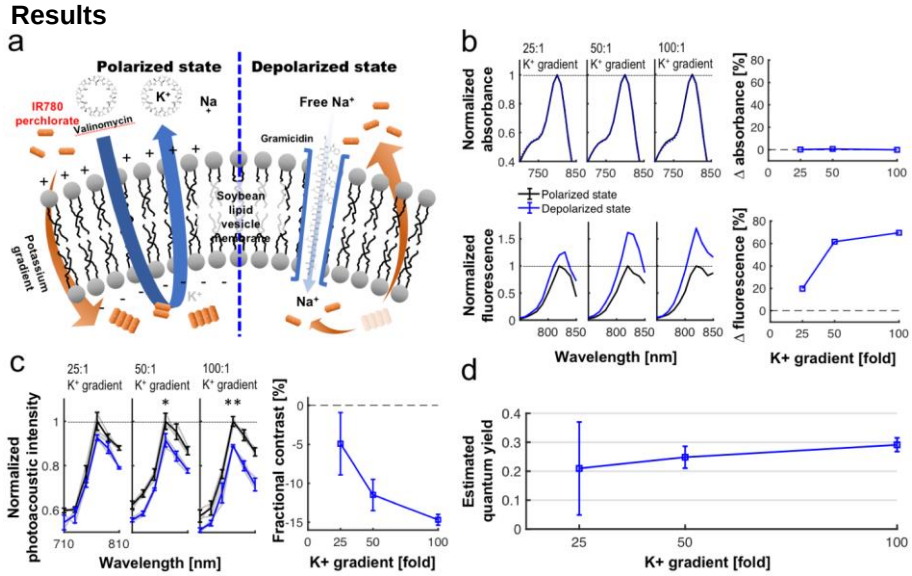

Fig. 3. VSD characterization using a lipid vesicle model. (a) Schematic diagram of a lipid vesicle model. (b) Fractional changes of the spectrophotometric and spectrofluorometric measurements in the polarized (black) and depolarized (blue) states. (c) PA intensity spectrum at 25-, 50-, and 100-fold K^+ gradients and fractional changes at 790 nm (p = 0.055, 0.010, and 0.002) between polarized and depolarized states for 25-, 50-, and 100-fold K^+ gradients, respectively. (d) The estimated quantum yield change for each K^+ gradient level [18]. The median values were presented in the estimated quantum yield range for each K^+ gradient level.

Fig. 3 presents the experimental results for a lipid vesicle model in various K^+ gradient levels. The membrane potential of soybean lipid vesicle model is manipulated by the valinomycin and gramicidin, by which the quantum yield change of VSD could accordingly triggered (Fig. 3a). From the spectrophotometric and spectrofluorometric measurements (Fig. 3b), the fractional change in fluorescence emission of the depolarized state over the polarized state were 19.70%, 61.63%, and 69.69% at -83mV, -102mV, and -120mV of membrane potential levels, respectively (i.e., 25-, 50-, and 100-fold K^+ gradient levels), while preserving a comparable level of absorbance: i.e., fractional absorbance change: 0.07%, 0.70%, and 0.21%, respectively. The fPA intensity change presented in Fig. 3c indicates the corresponding suppressive contrast in depolarized state from a polarized state: -4.91±4.00%, -11.49±2.00%, and -14.68±1.41% at -83mV, -102mV, and -120mV of membrane potential levels ($p < 0.005$). The expectable fPA contrast derived from the lipid vesicle experiments is -

12.24±1.18% / 100 mV. The quantum yield changes according to the given K^+ gradient levels were also estimated based on the theoretical model in our previous literature [18]. The median value in the estimated quantum yield range for each K^+ gradient level presents a proportionally-increasing trend as depolarized (Fig. 3d). Note that the non-specific quantum yield at 25-fold K^+ gradient is due to a limited sensitivity to differentiate the subtle membrane potential variation – The specificity of the estimation becomes proportionally improved as more K^+ gradient is given.

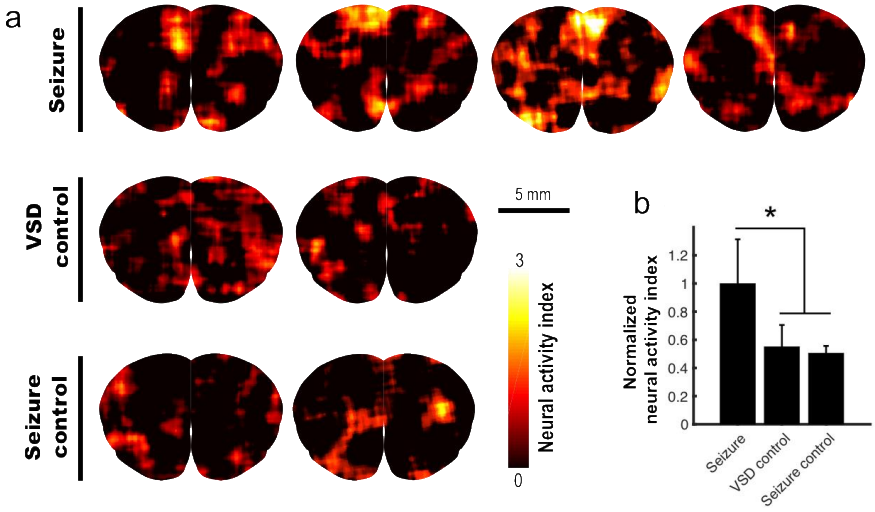

Fig. 4. *In vivo* transcranial fPA VSD imaging for seizure, VSD control, and seizure control groups: (a) The neural activity maps in each group. Note that each column indicates an individual rat included in each group; (b) The mean and standard deviation of neural activity index in each group. The region-of-calculation for each rat was extended to an entire brain region. The representative examples in ROI selections and corresponding fractional PA intensity change map are presented in Fig. 11 in appendix 5.2.

With the validated VSD mechanism, we conducted the *in vivo* validation for the transcranial fPA sensing of electrophysiological neural activity in the rat brain. The fPA probe imaged the coronal cross-section at bregma 2.2mm to cover the motor cortex where the seizure was confirmed by behavioral observation. Fig. 4a shows the neural activity maps projected for 10 min in each group to compare the activated brain regions among groups. All images have same range in neural activity index, i.e., 0.00–3.00. In the seizure group, the chemoconvulsant seizure induced substantial VSD responses, while the control groups revealed limited activity in cortical region throughout comparison phase. Fig. 4b compares neural activity indices in each group projected within whole brain region. Note that they were normalized by the mean value derived from the seizure group. As a result, the seizure group scored 81.3% and 97.9% more neural activity index than those in VSD control and seizure control groups. The seizure group indicated significant difference in comparison to the projection of the control groups: 1.00±0.31 (n = 4) vs. 0.53 ± 0.10 (n = 4); p = 0.05.

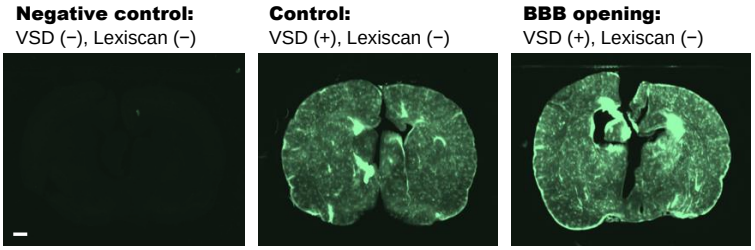

Fig. 5. Histopathological analysis on negative control (VSD-, Lexiscan-), control (VSD+, Lexiscan-), and BBB opening (VSD+, Lexiscan+) groups.

The appropriate VSD delivery into brain tissue was confirmed by the histopathological analysis on the harvested rat brains (Fig. 5). Three different groups were compared: (1) negative control group, VSD-/Lexiscan-; (2) control group, VSD+/Lexiscan-; and (3) BBB opening group, VSD+/Lexiscan+. The substantially-enhanced VSD uptake have been identified on the BBB opening group compared to that shown in the control group. The negative control group did not present any distinguishable fluorescence contrast. The result presents the effectiveness of BBB opening based on pharmacological adenosine receptor signaling modulation by regadenoson.

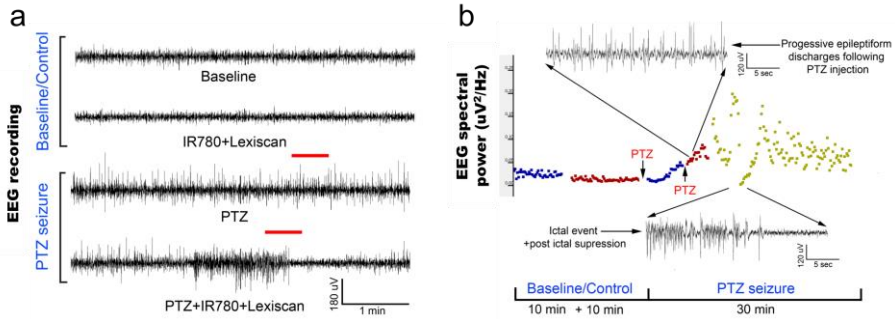

Fig. 6. Evolution of EEG signal in the *in vivo* protocol identical to transcranial fPA imaging: (a) Representative EEG traces recorded from rat motor cortex before and during induction of status epilepticus using chemoconvulsant PTZ. The baseline and control EEG traces represent EEG activity in an anesthetized rat (see methods) with and without IR780+lexiscan given at the dosage found to not alter baseline EEG activity in the pilot study. PTS seizure induction proceeded in classical style described previously wherein episodic epileptiform burst activity evolved into status epilepticus with intermittent occurrence of seizures and stable interictal activity. (b) EEG spectral quantitation of the EEG recording done every 10 sec epoch during the EEG showed the expected progression in EEG power associated with evolution of the PTZ induced status epilepticus. Time line of PTZ injections indicated with arrows. Expanded EEG traces on top show the uniform epileptiform discharges after following second PTZ injection and below a seizure event followed of post-ictal suppression indicating the termination of that event.

We validated the chemoconvulsant-induced seizure activity in the identical *in vivo* protocol with EEG recording. Using a well-established model of chemoconvulsant-induced *status epilepticus*, we replicated the classic evolution of chemoconvulsant-induced *status epilepticus* using PTZ (Fig. 6) [29]. These evolutions as related to bursts of synchronized neural activity *in vivo* were assessed by EEG using the experimental protocols mirrored from that of fPA imaging experiments. We recorded vEEGs of seizure inductions using PTZ (45mg/kg IP injections) in anesthetized rats. EEG baseline recording continued until a stable seizure induction profile (i.e., continuous burst discharges indicating synchronized neuronal depolarization-related action potentials) was recorded using sub-dermal EEG scalp electrodes. The seizure activity in EEG was associated with tonic-clonic movements in the fore- and hind-limbs of the anesthetized rats, indicating motor cortex involvement (Movie 1). The PTZ evolution of status on EEG did not alter with VSD treatment.

4. Discussion

Here, we present comprehensive characterization of our cyanine VSD mechanism using the lipid vesicle model, and a transcranial fPA imaging of electrophysiological neural activity *in vivo* using near-infrared VSD for rat seizure model with intact scalp. The near-infrared cyanine VSD, IR780 perchlorate, clearly revealed the mechanism-of-action for different

amount of depolarization (Fig. 3). Also, the proof-of-concept *in vivo* validation study demonstrated that the fPA imaging is capable of differentiating the generalized depolarization events in the seizure group from those in control groups (Fig. 4), which well agreed with EEG validation (Fig. 6). In addition, the pharmacological enhancement of VSD delivery into rat brain by increased permeability of the BBB was confirmed by histopathological validation (Fig. 5). These results demonstrate the feasibility of fPA VSD imaging without any needs for invasive procedures required in high-frequency PA neuroimaging.

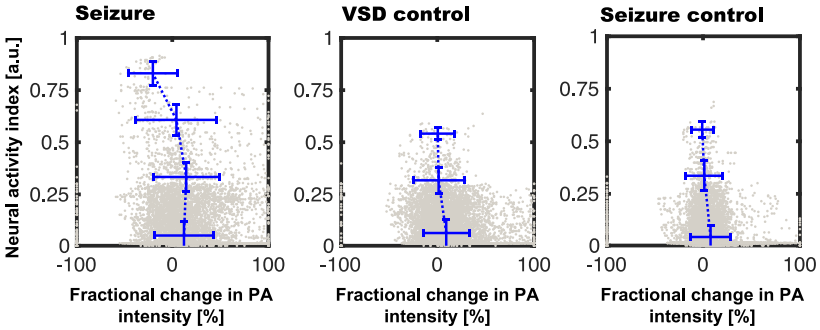

Fig. 7. Correlation of neural activity index to the fractional change in PA intensity between baseline and comparison phases. Pixels were categorized to four bins of distinct neural activity index ranges: 0 – 0.25, 0.25 – 0.5, 0.5 – 0.75, and 0.75 – 1.

The pixel-by-pixel correlation between neural activity index and the fractional PA intensity provided interesting perspectives (Fig. 7). Note that the first animal in each group shown in Fig. 4 was used for this analysis. In seizure group, the pixels presenting 2.25 to 3.00 of the neural activity index projected over 10 min indicated -20.94% of suppressive PA contrast, which corresponds to the VSD mechanism. Interestingly, not all the suppressive changes in PA intensity was converted into high neural activity index, which also validate a role of the normalized time-frequency analysis method to isolate the VSD response from the hemodynamic changes. Otherwise, the control groups did not present high neural activity index at the cortical region, whereas the seizure was also confirmed by behavioral observation in VSD control group. However, there was a case in seizure control group with unexpectedly localized yet high neural activity index at the primary somatosensory cortex region according to the rat brain atlas (the second rat case in Fig. 4). We hypothesize that neural activity might be real as the ketamine-xylazine does enable spontaneous and well as evoked cortical activity in anesthetized brains especially in periods after > 30 min following induction [38,39]. *In vivo* experimental protocol will be further regulated in our future investigation to reject any sensory interferences.

The potentially confounding factors for the *in vivo* experiments need to be carefully considered and eliminated. The change in CBV during chemoconvulsant seizure can generate proportional change of PA intensity that can be misinterpreted as the VSD response [40-42]. Zhang et al. suggested that time frame of the CBV change induced by chemoconvulsant seizure model: The time length of gradual CBV change from PTZ injection to seizure onset was ~2 min on average [43]. However, it was sufficiently covered by ~10 min of stabilization phase in our *in vivo* protocol (Fig. 1d). There is also an instantaneous hemodynamic change, but it was also rejected as described in the method section regarding our normalized time-frequency analysis with high-pass filtering at 0.2 Hz. Moreover, potential interference due to heart beating would not affect the results, as every individual fPA frame was compounded for two seconds that include 11–16 heart cycles of a rat (typically 5.5–8 beats per second).

The stability of stereotaxic fixation against the induced motor seizure was also investigated. The counter-hypothesis of this concern was an abrupt disorientation of rat brain due to motor seizure that will induce instantaneous decorrelation between adjacent PA frames. Also, based on the behavioral observation during seizure, we anticipated the

decorrelation within a sub-second time scale, if it happened. For these hypotheses, we calculated the cross-correlation maps throughout PA frames obtained from 2 min to 8 min (1920 frames, 240 frames/min). Three different time intervals for decorrelation calculation were tested: 0.25 sec, 0.5 sec and 1 sec, which respectively correspond to 1, 2 and 4 frame intervals (Fig. 8). From the minimal correlation projection (MCP) map projected in entire temporal direction, motor seizure did not yield a significant decorrelation in the adjacent PA images when comparing to normal condition for the given time period. Even with 1 sec of interval, baseline and seizure phases present consistent minimal correlation value in the brain tissue region: 0.53±0.04 vs. 0.54±0.04, respectively. Therefore, the interference by motor seizure could be rejected as potential cause of artifacts in the results.

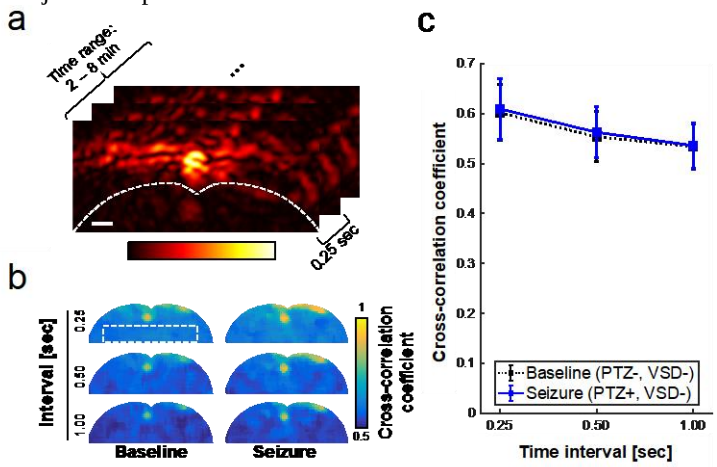

Fig. 8. Minimal correlation projection (MCP) image using cross-correlation coefficients with varying time interval, i.e., 0.25 sec, 0.5 sec, and 1 sec, which respectively corresponds to 1, 2, 4 frame intervals with the imaging rate at 4 frames per second. (a) region of interest for the inter-frame cross-correlations, (b) MCP images of baseline (PTZ-, VSD-) and seizure groups (PTZ+, VSD-) for brain tissue region. (c) Cross-correlation coefficient for varying time intervals.

Toxic CNS effects of VSD is another factor that alters brain activity. We tested our protocols with varying VSD concentration in rats as a direct application to the cortex. Rats were anesthetized with IP injection to ketamine/xylazine and a cranial window made over the right motor cortex. After recording a baseline EEG in the rat for 10-min duration with the craniotomy, the follow-on EEG recording continued to record EEG following application of increasing concentrations of vehicle alone and VSD + vehicle for the same duration of EEG recordings (i.e.; 10 min) allowing comparisons of EEG responses to each increasing gradient of VSD on cortical activity as compared to baseline EEG signature in the same rat. Results for VSD with cortical application with cranial windows used in six male rats yielded reliable and reproducible EEG signatures for each concentration (Fig. 9). This protocol identified that VSD concentrations had no effect in altering the baseline EEG in the same rat, indicating no toxic effect on cortical circuit function. Direct cortical application with 100X VSD resulted in significant EEG background suppression in 4/6 rats, indicating that the certain concentrations of VSD could alter baseline circuit function in the motor cortex. This EEG suppression was recovered to baseline over the 10-min recording period, indicating that the transient effect from the time of application as the 100X VSD either diluted or cleared out of the focal application zone over the 10-min period. We reject the toxic CNS effects of VSD as we used 10X concentration based on this result.

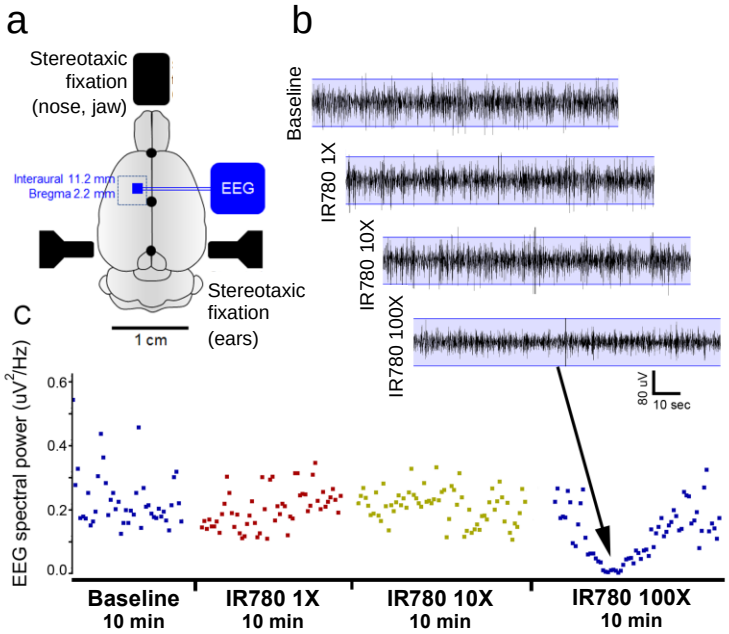

Fig. 9. VSD toxicity study using EEG recordings during direct cortical applications using a cranial window in rats. (a) Schematic of experimental protocol. A rectangular cranial window drilled under anesthesia overlying unilateral motor cortex. Duramater was kept intact. Following craniotomy, a small window was made in duramater without traversing blood vessels. (b) EEG recording of baseline brain activity under anesthesia was followed by using a hamilton micro syringe to apply increasing concentrations of IR780 directly to the cortical surface via window made in duramater. Base EEG remained unaltered at lower concentrations but showed significant background suppression after applying a 100X solution. This study allowed us to determine the concentration of IR780 10X for all PA experiments. (c) EEG power spectral quantification for every 10-sec epoch of EEG over the duration of the recording confirmed EEG suppression with the 100X dose.

We plan a number of follow-up efforts to further advance the concept. We will further regulate the experimental protocol, including possible visual or audible perception for rats during the experiments, and also collect more *in vivo* data sets. In addition, there would be several improvements in imaging system: using 2-D PA probe would provide the most reliable setup as it enables the absolute positioning of specific brain parts. Also, the sensing speed of our current fPA imaging system would be improved. Current fPA sensing speed is limited to 4 frames per second to obtain sufficient signal sensitivity in the deep brain cortex region. This speed may limit its applicability in research, as it is well known that resting electrophysiological neural activity ranges up to several tens of Hz (e.g., delta: 1–4Hz; theta: 4–8Hz; alpha: 8–13Hz; beta: 13–30Hz; gamma: 30–80Hz). Having another dimension in spectral dimension would be beneficial to quantify the VSD response and hemodynamic changes at the same time. Successful improvements will substantially increase the capability to understand brain circuit functionality in real-time using the proposed fPA imaging technology.

The toxicity and biodegradability of our VSD is an important issue that deserves further evaluation; Even though there have been no long-term and comprehensive toxicity study, we believe that the metabolic products of IR780 perchlorate should be very similar to ICG, FDA-approved near-infrared cyanine dye, as they are basically comprised by same chromophore. This strongly suggests its biocompatibility with our VSD mechanism. We will further prove our hypothesis in our future works.

Furthermore, the integration of localized neural stimulation methods to our fPA imaging will allow us to substantially elevate our understanding on how brain respond to a controlled stimuli [44]. In particular, we envisage that the glutamate receptor modulation and/or direct stimulation on sensory cortex can be studied, and we have recently obtained encouraging results in NMDA-evoked cortical [45] and physiological neural activity imaging at visual cortex with visible light stimulation [46]. In addition, the integration with ultrasound neuromodulation may have a huge impact on the neuroscientific and clinical efforts by enabling the breakthrough beyond the passive brain investigation, while allowing additional benefits on non-pharmacological BBB opening [47,48].

Acknowledgements

Authors thank Dr. Abhinav K. Jha for proof reading the manuscript and providing helpful comments. Also, authors thank Drs. Diane S. Abou and Daniel L. J. Thorek for providing equipment and facilities for lipid vesicle experiments with helpful comments. Financial support was provided by the NIH Brain Initiative under Grant No. R24MH106083-03 and the NIH National Institute of Biomedical Imaging and Bioengineering under Grant No. R01EB01963. Jeeun Kang, Ph.D. is supported by Basic Science Research Program through the National Research Foundation of Korea (NRF) funded by the Ministry of Education (2018R1A6A3A03011551).

Appendix

4.1 Characterization of imaging performance.

The performance of the PA imaging system was evaluated. The wire target with 150-µm diameter was placed in the water tank, and the PA data were obtained at 20-, 25-, and 30-mm distance which are in the depth-of-interest for our lipid vesicle and *in vivo* experiments. The data recording was also extended for 10 min to validate the expectable range of pulse-to-pulse laser energy fluctuation. Fig. 10a presents the full-width-half-maximum (FWHM) measurements were 473.0 µm, 477.8 µm, and 482.6 µm (479.5 ± 2.7 µm in average) in axial direction, and 448.5 µm, 467.6 µm, and 496.2 µm (470.8 ± 24.0 µm in average) in lateral direction at 20 mm, 25 mm, and 30 mm depths, respectively.

We also evaluated the short- and long-term laser energy variation; Fig. 10b shows the energy fluctuation when various number of frame averaging is applied: 1, 5, 10, 20, 40 frames. The result proves that the median values were well converged to baseline: 0.10%, -0.07%, 0.06%, 0.14%, and 0.10% of fractional change from the global mean value, respectively. Also, the lower and upper adjacent values were limited well with more frame averaging: -8.69 – 8.69, -5.17 – 5.13, -4.52 – 4.86, -3.30 – 4.34, and 2.01 – 3.02 for 1-, 5-, 10-, 20-, 40-frame averaging, respectively. Note that our image reconstruction was with 40-frame averaging. *In vivo* signal fluctuation was much greater than error given by laser fluctuation (raw PA intensity sequence in Fig. 2). In the investigation on long-term laser energy variation, the fractional PA intensity change was only 0.15% between the first and last two minutes: 0-2 min: 0.00±1.27% vs. 8-10 min: 0.15±1.33 % (Fig. 10c). In addition, there was no significant photo-bleaching detected with given energy density, 3.5mJ/cm^2 (Fig. 10d).

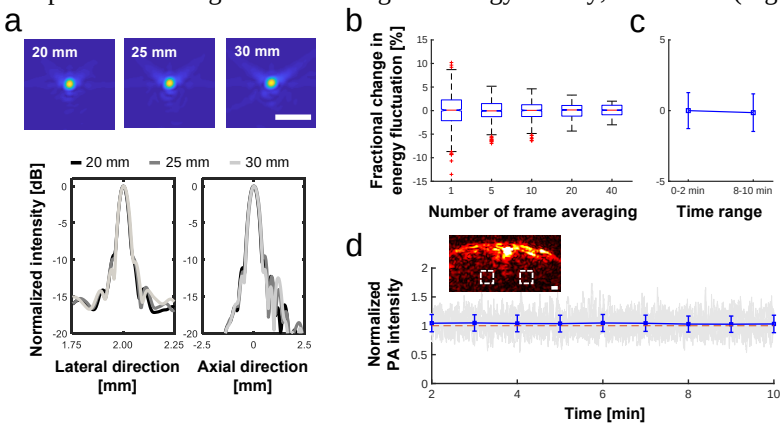

Fig. 10. PA imaging characterization: (a) spatial full-width-half-maximum (FWHM) beam profile in axial and lateral directions at various depth-of-interest (i.e., 20, 25, and 30 mm). (b) Fractional change in energy fluctuation with various number of frame averaging (i.e., 1, 5, 10, 20, 40 frames). (c) Long-term comparison in laser energy fluctuation between 0-2 min to 8-10 min time ranges. (d) Normalized PA intensity for 8 min. PA intensity averaged for 1-2 min was used as a reference intensity. White dotted rectangular in the PA image of seizure control rat indicates the photo-bleaching ROIs.

4.2 ROI selection for neural activity index reconstruction.

Fig. 11 presents the representative examples in ROI selection for neural activity index reconstruction based on the anatomic relationship between SSS and brain tissue. Whole brain tissue region was selected using a rat brain atlas at bregma 2.2mm as used in the *in vivo* experimental setup. The fractional change of PA intensity at 790 nm between comparison and baseline phases were also presented (second row), which demonstrate the seizure-induced

CBV change. Note that the PA image was projected in last 5 min for both comparison and baseline phases.

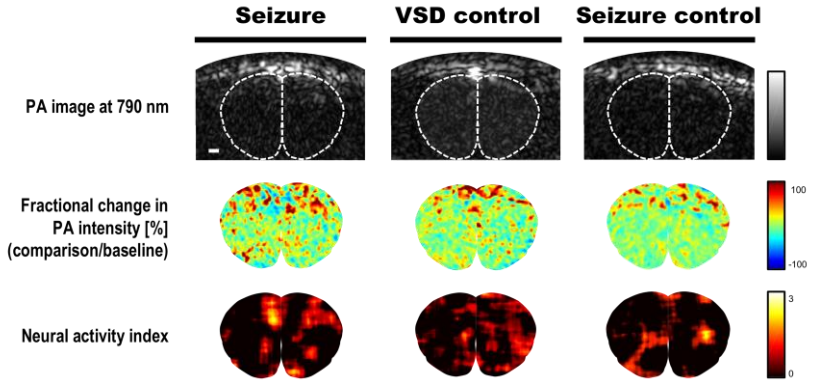

Fig. 11. Representative examples in ROI selection for neural activity index reconstruction and its correlation to the corresponding fractional change in PA intensity from baseline to comparison phases.